Novel correlative microscopy approach for nano-bio interface studies of ultrafine particle-induced lung epithelial cell damage

Rok Podlipec[1,2], Luka Pirker[2,3], Ana Krišelj[2], Gregor Hlawacek[1], Alessandra Gianoncelli[4], Primož Pelicon[2]

[1] Helmholtz-Zentrum Dresden-Rossendorf e.V., Institute for Ion Beam Physics and Materials Research, Bautzner Landstrasse 400, 01328 Dresden, Germany

[2] Jožef Stefan Institute, Jamova cesta 39, 1000 Ljubljana, Slovenia

[3] J. Heyrovský Institute of Physical Chemistry, v.v.i., Department of Electrochemical Materials, Dolejškova 3, 182 23 Prague 8, Czech Republic

[4] Elettra, Sincrotrone Trieste, Strada Statale 14 - km 163,5 in AREA Science Park, Trieste, Italy

E-mail: rok.podlipec@ijs.si

Abstract

Correlative light and electron microscopy (CLEM) has attracted widespread interest in the life sciences community, particularly in light of recent developments in imaging resolution and sensitivity, and sample preservation. One of the highly relevant scientific areas that can be addressed by CLEM is nanotoxicology, the study of the environmental and, in particular, health effects of the ubiquitous particulate matter in polluted air. To assess safety and predict outcomes, particularly those induced by highly penetrating ultrafine particles (UFPs), it is invaluable to understand the mode of action at the molecular level, from the moment the particles interact with lung tissue. In our study we address these challenges by combining novel multimodal high-resolution live and fixed cell microscopy, from fluorescence lifetime imaging microscopy (FLIM), hyperspectral fluorescence imaging (fHSI), scanning electron microscopy (SEM), ultra-high resolution helium ion microscopy (HIM) to synchrotron micro X-ray fluorescence (SR μXRF). These provided a comprehensive insight into the structural and functional properties of the nano-bio interface formed on the surface of lung epithelial cells exposed to titanium dioxide nanotubes (TiO_2 NTs) and for the first time, we report several important initial cellular responses. Besides the characterization of extensive biomolecule binding to TiO_2, including DNA and its accumulation-related plausible implications for apoptosis and inflammation, we show acute changes due to fibrin-like fibrous network formation over aggregated nano-bio composites and accumulated iron-induced changes in the molecular environment at the nano-bio interface. The

applied CLEM approach demonstrates high applicability for studying the initial cellular responses to nanoparticles, which can play a crucial role in the body's immune response and the development of inflammation. The methodology provides a robust framework for future research into nanoparticle toxicity and its impact on human health.

Keywords: high-resolution correlative light and electron microscopy (CLEM), fluorescence lifetime imaging microscopy (FLIM), fluorescence hyperspectral imaging (fHSI), synchrotron micro X-ray fluorescence (SR µXRF), helium ion microscopy (HIM), CLEM-µXRF, ultrafine particles, TiO_2 nanotubes, nanotoxicity, lung epithelium

1. Introduction

Among the novel microscopy approaches, correlative light and electron microscopy (CLEM) has attracted considerable interest in the life sciences community, particularly following recent developments in the spatial resolution capabilities of light microscopy and the cryogenic capabilities of electron microscopy [1,2]. Advanced imaging of live cells, with its targeted labelling of individual cellular components, can provide molecular specificity and the observation of dynamic changes [3,4]. In addition, the advanced imaging of fixed cells, when performed in high vacuum, can provide ultrastructural information with nanometer spatial resolution [5] and chemical information with sub-micron resolution [6,7]. When successfully combined on the same region of interest (ROI), a correlative microscopy (CM) approach offers several significant advantages. It provides comprehensive functional and structural insights at multiple scales, as well as increased accuracy through cross-validation of data and improved contextual understanding through the analysis of dynamic and static processes on live and fixed cells, respectively.

One of the highly relevant scientific areas that can be addressed by CM is the field of nanotoxicology, which studies the environmental and, in particular, health effects of the ubiquitous particulate matter in the polluted air [8]. In particular, ultrafine particles (UFPs) less than 100 nm in size can penetrate deeply into the lungs and induce a variety of chronic diseases, including inflammation, fibrosis and cancer [9,10]. For safety assessment and prediction of UFPs-induced adverse outcomes, understanding of the mode of action at the molecular level, starting from the moment the particles interact with the lung tissue, is critical. To this end, several innovative CM approaches have been introduced in recent years to elucidate the interaction at the nano-bio interface and the subsequent impact of nanomaterials and/or elements on biological matter [11–34]. The CLEM approach is typically applied by combining conventional light microscopy (LM) with

electron microscopy (EM) [11], and in particular by combining more specific and targeted fluorescence microscopy (FM) with transmission electron microscopy (TEM) [12–14]. More recently, super-resolution fluorescence imaging in combination with TEM and scanning electron microscopy (SEM) has been implemented to address the complex biological questions at the nanoscale [15]. However, studies are not limited to CLEM alone and several other approaches have been developed in recent years. These combine fluorescence microscopy with X-ray tomography, dark-field microscopy (DFM), atomic force microscopy (AFM) [16–19] and even the combination of several, optical, electron and ion-based techniques [20,21]. To allow more detailed and quantitative analysis of the specific molecules and elements present in biological tissues, CM approaches often include secondary ion mass spectrometry (SIMS) combined with electron microscopy [22–24] and novel high-resolution helium ion microscopy (HIM) [25–27]. In addition to SIMS, proton-induced X-ray emission (PIXE) and X-ray fluorescence (XRF) analytical techniques are also used to quantify chemical elements in biological samples, and are combined with FM [28] and EM [29,30], respectively. Other correlative approaches include combination of XRF with AFM [31] or XRF with ion beam techniques [32–34] for elemental quantification and complementary information.

Despite the continuous development of new CM approaches in this specific field of research, the full potential of multimodalities and their combinations has not yet been fully exploited. In this study, we present a novel pipeline in the field of correlative microscopy that addresses relevant toxicological questions regarding the mechanisms of interaction of UFPs, in our case inflammatory [35] and potentially carcinogenic [36] titanium dioxide nanotubes (TiO_2 NTs), with lung epithelial cells. We demonstrate the utility of an innovative multimodal and multiscale experimental workflow that integrates several complementary and complementing imaging and spectroscopy techniques on live and fixed cells in a high vacuum (Fig. 1). In order to preserve the nanoscale morphology and properties of the investigated nano-bio interfaces on the surfaces, we use a rapid cryofixation technique without chemical cross-linking, which could otherwise compromise sample size, shape or cell membranes at the investigated spatial scale [37–41]. We must acknowledge that the development of sample preparation and preservation for high-vacuum, high-resolution CM is one of the major challenges in CM and can play a key role in influencing the physicochemical properties of samples and the subsequent interpretation of results [7,31,32,42].

The present study aims at covering a wide range of detectable spatial scales (down to the nanometer level) and to gain insight into both functional and structural properties of the samples under investigation. In order to obtain comprehensive knowledge, data gathered from multimodal fluorescence microspectroscopy performed on living cells were integrated with data obtained from

high resolution and high elemental-sensitivity X-ray, electron and ion-based techniques performed in high vacuum. These approaches provided new insights into the physicochemical properties of cell-excreted and cell-deposited nanomaterial-biological matter (nano-bio) composites aggregated and anchored on the surface of the lung epithelium. In addition, further insights were gained into the mechanisms of the transport and binding of DNA molecules to UFPs, as well as into the mechanisms of fibrous network formation over UFPs, indicating an acute cellular response. These findings contribute to a deeper understanding of the current knowledge in the field of UFPs-induced nanotoxicity on the lung epithelium.

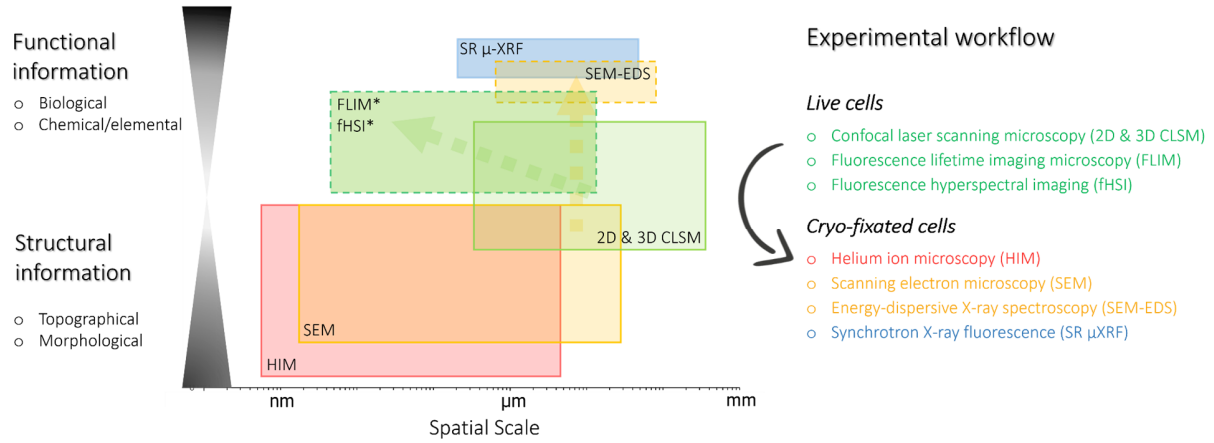

Fig. 1. Novel multimodal microspectroscopy-based correlative microscopy (CM) covers broad spatial scales ranging from several tens of microns down to nm for a detailed functional and structural investigation of the nano-bio interface of lung epithelial cell response to ultrafine particles (UFPs). Typical imaging ranges for each technique, with the type and extent of information provided, are shown within the colored areas. * Spatial scale extended below optical resolution limit as FLIM and fHSI can sense molecular interactions.

2. Results and discussion

2.1. Correlative multimodal fluorescence microscopy and SEM-EDS (multimodal CLEM) reveals new insights into the transport and interaction of DNA with exposed TiO_2 nanotubes during apoptosis in lung epithelial cells

To gain new insights into the interaction between lung epithelial cells and ubiquitous metal oxide TiO_2 nanoparticles, we first performed imaging and analysis on live cells exposed to TiO_2 NTs for 2 days. By employing an integrated advanced microscopy instrumentation, we conducted

multimodal high-resolution fluorescence imaging (Fig. 2A-B). The cells were grown on special, 10 nm thin Finder grid Formvar/Carbon substrates with fiducials employed for correlative microscopy (Fig. 2A, arrow). Prior to measurement, each cell structure was stained with a different fluorescence dye. In the presented case, the mitochondria, actin network and nuclei were stained to characterize any potential structural and/or functional changes that may have occurred as a result of exposure to nanoparticles. To track and determine potential co-localization between cellular structures and nanoparticles, TiO_2 NTs were fluorescently stained prior to administration according to the well-established protocol [43]. Two-channel confocal laser-scanning microscopy (CLSM) was employed, utilizing pulsed, ps excitation lasers at 561 nm and 640 nm, in combination with two avalanche photodiode detectors. Initially, low-magnification imaging was conducted using a 10X objective, with the aim of identifying the fiducials that are essential for successful registration and overlap of CM images. In addition to the clear visualization of the grid (Fig. 1A, in black), it was possible to distinguish between TiO_2 (in red) and mitochondria (in green). To gain further insight into the interaction between TiO_2 with cells, high-resolution imaging in three dimensions (3D) was performed using a 60X magnification (Fig. 1A, second image). The 3D image reveals the localization and aggregation of TiO_2 on the cell surface (white arrow), a phenomenon observed and described in our recent study [35]. Here, we observe heterogeneity in the morphology and the size of formed nanomaterial composites (upper image section (UP)). Nevertheless, the close excitation and emission profiles of fluorescent dyes prevented the differentiation between the TiO_2, nucleus and actin structures found beneath the cell membrane (lower image section (LOW)), using a 2-channel CLSM.

To better characterize these individual structures, we then proceeded with fluorescence lifetime imaging microscopy (FLIM), which was integrated into the same experimental setup. FLIM, being a powerful and valuable imaging technique for measuring the lifetime of fluorescent molecules independently of signal intensity [3], can provide quantitative information about properties and changes in the molecular environment, thus enabling the study of molecular interactions [44]. FLIM was capable to reveal the individual labeled structures (Fig. 2B), which was not possible with multichannel imaging presented in Fig. 2A. The fluorescence lifetime, as measured in each image pixel, is color-coded with the mean lifetime (τ_m), which represents the weighted average of the individual lifetime components (τ_i) from the bi-exponential fit (Equation 1). The FLIM analysis performed after utilization of a single excitation laser source at 640 nm enabled the distinction between actin structures (depicted in blue), a nucleus undergoing a distinct phase separation due to specific biophysical and/or biochemical processes [45] (depicted in

orange), and TiO_2 with a wide τ_m distribution (shown in green to yellow). The latter could indicate a high degree of structural and molecular variability, with the potential for local attachment of DNA molecules and/or their fragments to nanoparticle composites (illustrated by the arrows). The proximity of the Draq5 dye, intercalated in the DNA structure at a distance of below 10 nm to the Alexa Fluor 647 dye attached to TiO_2, could induce a fluorescence resonance energy transfer (FRET) transition, which is known to shorten the fluorescence decay time [46]. This is demonstrated in our study with blue shift in τ_1 and τ_2 distribution locally (Fig. 2B, right upper image). The observed presence of DNA signal in conjunction with the distinctive round-shaped structures is also consistent with the known occurrence of DNA and rRNA in extracellular vesicles (EVs), large microvesicles, and apoptotic bodies [47].

To gain further insight into the structural and functional properties of the formed composites, we then prepared the samples for correlative SEM (Fig. 2C). Due to the chemical fixation treatment 4% PFA and 2% GA and the fragile thin formvar/carbon support films, there was a slight displacement of the investigated cell and its structures as indicated by the arrow. However, in this specific study, this was not an issue, as it was sufficient to identify the same EVs on fixated cells and perform further morphological and chemical characterization (Fig. 2C-D). The SEM measurements revealed the presence of distinct morphological features of large EVs, which exhibited a resemblance to apoptotic bodies. An additional SEM-EDS chemical mapping (Fig. 2D) with typical spectra (Fig. S1 in SI) revealed that rough topography was co-localized with the presence of TiO_2 (Ti map in green), while all large EVs exhibited a similar amount of biological matter (C map in yellow). A thinner layer of biological matter in TiO_2-rich EVs indicates a more concentrated accumulation and binding of lipid and protein to TiO_2 nanoparticles, as observed in our recent study [48]. With a detailed chemical analysis of the distinct regions marked with 1-3 we were also able to address the previous observation, via FLIM analysis, about very likely presence of DNA in EVs. The results, expressed as bar charts normalized to the nitrogen concentration, clearly demonstrate that the content of P and Na relative to the content of biological matter (N) is more than three times higher inside EVs (regions 2 and 3) than in the surrounding cell membrane (region 1). It is noteworthy that there was no discernible difference in P concentration between EVs with varying TiO_2 abundance, suggesting that the DNA or its fragments present in both cell-excreted structures may have a similar content. Among the elemental composition, only Na content was found to be significantly higher in the EVs with TiO_2, indicating a potential for preferential Na ion adsorption on the TiO_2 surface, as previously reported [49].

With the CM approach, we gathered a more detailed structural and functional information about the large EVs formed on the surface of lung epithelial cells exposed to TiO_2 NTs. The results of subsequent analysis performed on live and fixed cells imply on a high DNA content in large EVs, which together with the morphology suggests the presence of apoptotic bodies. Furthermore, the initiation of cell apoptosis could well be displayed through the nuclear condensation observed in Fig. 2A (bottom right image) [50]. It might be even possible that the observed irregularly shaped 'apoptotic bodies' packed with TiO2, which are anchored on the cellular surface induce defects and prevent apoptotic cell clearance. If our hypothesis is true, the defects could initiate the progression of a number of pathological conditions, such as inflammation or autoimmunity [51].

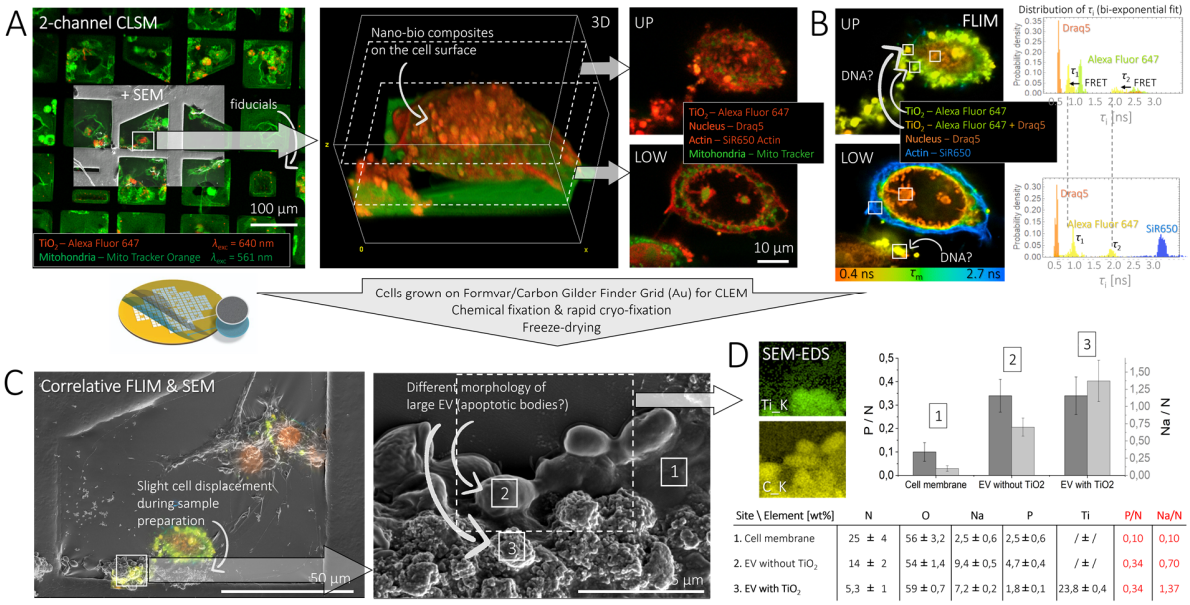

Site \ Element [wt%]	N	O	Na	P	Ti	P/N	Na/N
1. Cell membrane	25 ± 4	56 ± 3,2	2,5 ± 0,6	2,5 ± 0,6	/ ± /	0,10	0,10
2. EV without TiO_2	14 ± 2	54 ± 1,4	9,4 ± 0,5	4,7 ± 0,4	/ ± /	0,34	0,70
3. EV with TiO_2	5,3 ± 1	59 ± 0,7	7,2 ± 0,2	1,8 ± 0,1	23,8 ± 0,4	0,34	1,37

Fig. 2. Correlative multimodal fluorescence microscopy and SEM-EDS (multimodal CLEM) applied on lung epithelial LA4 cells exposed to TiO_2 NTs reveals morphological changes at the interface and the insights of DNA transport. A) Nano-bio composites on the cell surface together with the morphology of external and internal structures of cell nuclei, actin and TiO_2 (in red) and mitochondria (in green) performed by 2D and 3D CLSM using 10X and 60X magnification objectives. B) The same structures characterized with FLIM modality capable of distinguishing between individual labeled structures (color coded from red, indicating a short decay time, to blue, indicating a long decay time) using the same laser source (λ = 640 nm). Shifted distribution of τ_1 and τ_2 from bi-exponential fit (green to yellow in the chart on the right) indicate on local FRET between TiO_2 and DNA dye revealing potential binding of DNA to nanoparticles. C) Correlative FLIM and SEM performed on the same site after a successful registration and overlap of fiducials shown in A). High magnification reveals different morphologies of large EVs denoted with 2 and 3. D) Chemical

characterization of the same structures performed by SEM-EDS confirms not only the presence of biological matter (C_K) on nanoparticles (Ti_K) but also a few times higher content of P (right chart and table) suggesting a high DNA load inside large EVs which resemble an apoptotic body.

2.2. In-depth physico-chemical characterization of TiO_2 NPs-rich cell-excreted composites with biological relevance using novel multimodal CLEM combined with synchrotron μ-XRF (CLEM-μXRF)

To gain further insight into the morphological and structural properties of TiO_2-induced nano-bio composites formed on the cellular surface, as well as to gain further insight into their chemical properties at the sub-micron scale, we implemented a novel correlative microscopy approach. We applied additional fluorescence hyperspectral imaging (fHSI) (Fig. 3C, right column) on live cells to support CLSM (Fig. 3B) and FLIM measurements (Fig. 3C, left column) from the same site. To enhance the quality of the imaging capability and sample preservation, we employed special 100 nm thick silicon nitride (Si_3N_4) substrates/windows (Fig. 3A) transparent for soft X-rays, which were used in our novel CM pipeline and avoided chemical fixation to maintain the nanoscale features of the investigated surface structures (Fig. 3D), respectively. To enhance the sensitivity and resolution of elemental analysis, we expanded the CLEM approach presented in Fig. 2 by integrating correlative synchrotron spatially-resolved SR μXRF (Fig. 3E-F). Its capacity for sub-micron resolution and high elemental sensitivity makes it a valuable tool for investigating intricate biological processes [52].

After the required period of cell growth on a surface-modified Si_3N_4 substrate with fiducials in the form of multiple 100 x 100 μm transparent windows, lung epithelial cells were exposed to fluorescently labelled TiO_2 NPs for a period of 3 days. Observation of numerous objects, measuring up to several microns in size, revealed a high concentration of TiO_2 NTs, shown in green using wide-field FM (Fig. 3A). The labelling process was carried out in a way that avoided the introduction of artefacts, using Alexa Fluor 647 in according to the protocol recently developed by our research group [43]. The cells were then stained with the in-house PSM-39 dye, which is used to label the lipid droplets. As a result of the partitioning of the dye to other lipid-rich environments during the incubation period, the contrast of the lipid droplets (LD) was reduced, as evidenced by the orange staining (Fig. 3A). To improve the resolution, two-channel confocal laser scanning microscopy (CLSM) was performed according to the methodology described above. The same site is indicated by a white rectangle and color-coded with red (TiO_2 NTs) and green (LDs and cell membranes). The confocality allowed significantly improved contrast and resolution of

the size distribution and shape of the TiO_2 NTs-rich composites, ranging from yellow to red, indicating different degrees of membrane molecule wrapping around the particles. The composites appear to have a nearly round shape and a size of up to 5 µm (white arrow).

To obtain further information on the local properties and interactions in the immediate vicinity of the observed TiO_2 NTs-rich composites and lipid droplets, with an improved contrast, we performed FLIM and fHSI imaging/mapping at the same site (Fig. 3C). The two structures are shown within rectangles, showing typical and easily distinguishable FLIM and fHSI signals. fHSI of LDs and lipid-rich regions revealed up to 10 nm spectral shifts (660 - 670 nm, purple to blue, white arrow), indicating local microenvironmental differences, such as molecular conformation, polarity, etc. [53]. In addition, changes in FLIM were observed, with LDs showing a reduced mean fluorescence lifetime (τ_m) (light blue) compared to other lipid-rich regions (dark blue), indicating their increased packing density. Analysis of TiO_2 NPs-rich composites showed less heterogeneity, but still with a considerable range in τ_m, spanning from 0.6 to 1.0 ns, also indicating on differences in the packing density. An increased τ_m may indicate a greater distance between fluorophores, possibly due to lipid interspacing [35]. In addition, we present typical examples of fluorescence decay curves and fluorescence spectra for the voxels within the regions shown. These curves have been fitted with a bi-exponential function (Equation 1) and an empirical intensity-normalized log-normal function with nanometer peak position resolution [54], respectively.

In order to support a detailed, time- and spectral-resolved analysis of the interaction between TiO_2 NTs and biological matter, performed on living cells, we applied a novel correlative microscopy approach involving the introduction of a combination of SEM and SR µXRF (Fig. 3D-F). These techniques provided insights into the nanoscale morphological and structural features and sub-micron elemental properties. The use of a 150 mM ammonium acetate wash solution to remove buffer salt crystals, which otherwise interfere with structural and chemical analysis [55], followed by rapid cryofixation by plunge freezing and final lyophilization, allowed the preservation of the majority of cell surface structures, including the studied TiO_2 NPs-rich excreted composites (Fig. 3D, white arrow). The highest magnification SEM image shows that the particle is almost completely spherical in shape. This shape is the most efficient packing with the lowest surface energy, thus providing the highest stability [56]. The observed shapes are consistent with the fluorescence signal from the same site, as measured by CLSM on live cells (Fig. 3B, white dashed region). To obtain further biological information on the spherical composites, the same sample was transferred to a synchrotron facility and elemental imaging using SR µXRF with the typical spectral acquisition and fitting was performed (Fig. 3E) together with scanning transmission X-ray

microscopy (STXM) [52] for simultaneous absorption/atomic number contrast on the same cell. In addition to confirming a high TiO_2 content within the spherical composites, as evidenced by locally elevated concentrations of O (K-line spectra) and Ti (L-line spectra), we also observed a higher content of C, N, Mg and, partially Na (all K-line spectra) at the same sites. This directly reveals an extensive binding of biomolecules, such as lipids, to the surface of the TiO_2 NTs and validates our recent findings performed on the same exposed nanoparticles using a combination of *in vitro* measurements and *in silico* simulations [35]. The local increase in Na adsorption may be due to the local crystallinity of the TiO_2 anatase surface [57] or, alternatively, it may bind preferentially to highly negatively charged biomolecules such as heparan sulphate (HS), the molecule found on cell surfaces and which plays a central role in inflammatory processes [58]. The good co-localization of the elevated Na with the filamentous structures bridging the spherical composites, as observed by SEM (Fig. 3E, purple arrow in the lower image), may be indicative of HS-induced inflammatory activity. However, further molecular studies are required to confirm this hypothesis. Finally, the physicochemical characterization of the cell-excreted structures is summarized in a single image (Fig. 3F). The typical structures and features of the nano-bio composites are presented with color-coding, as indicated by the arrows.

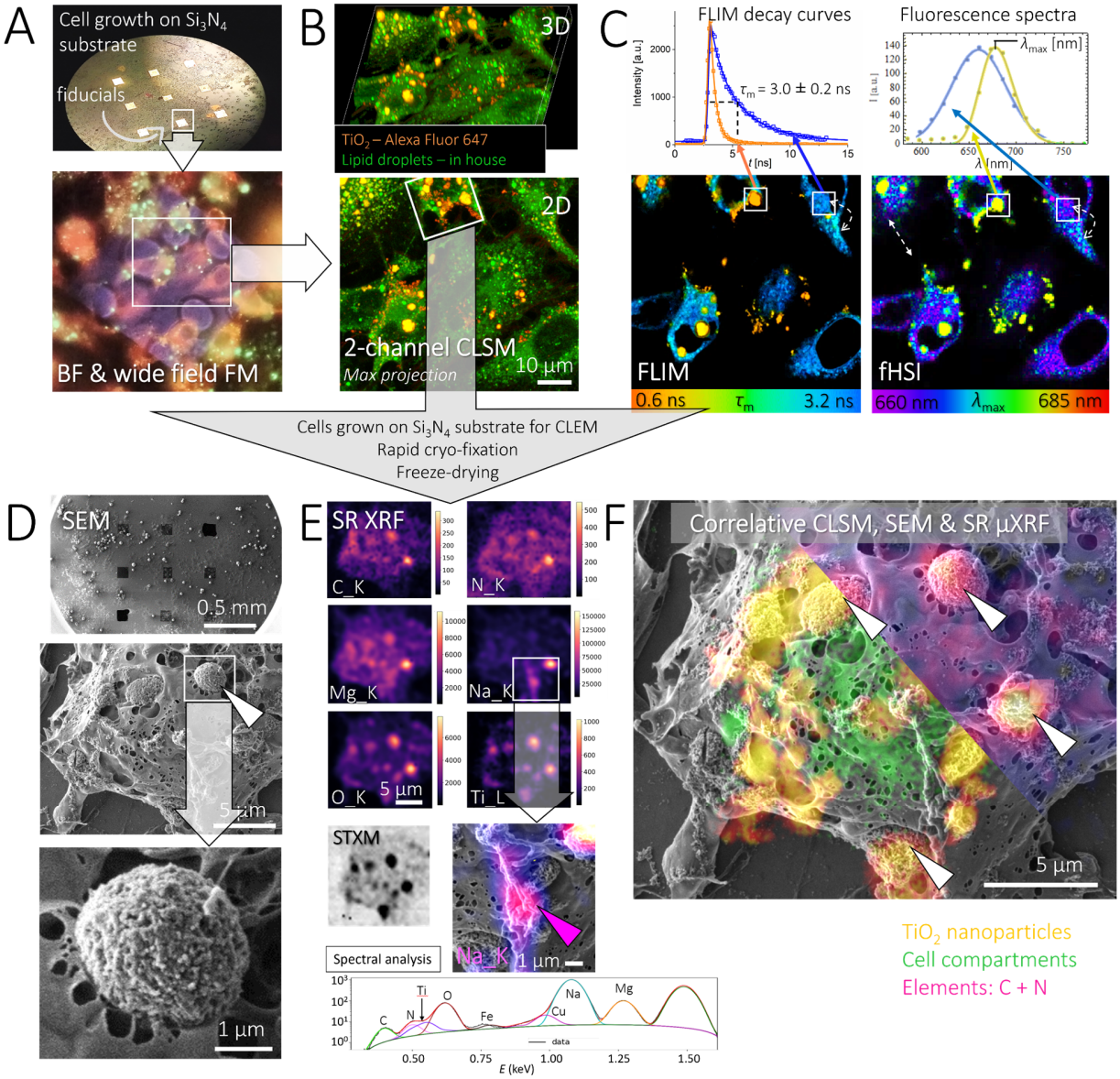

Fig. 3. Novel multimodal CLEM combined with synchrotron µXRF (CLEM-µXRF) revealing in-depth physico-chemical properties of TiO_2 NPs-rich cell-excreted composites formed on lung epithelial LA4 cells. A) Combined wide field FM and BF employed to visualize cell growth on 100 nm thick transparent silicon nitride (Si_3N_4) substrates of the 100*100 um dimension used as fiducials and with optimal compatibility for the correlative microscopy in a transmission mode (µXRF). B) 2D and 3D CLSM performed on the same site show labeled cells (in green) and cell-excreted TiO_2 composites (in orange). C) The same site characterized with FLIM and fHSI modalities, capable of distinguishing between individual labeled structures and of inspecting local microenvironment differences, such as molecular conformations and polarity [53]. The upper charts illustrate typical FLIM decay curves and fluorescent spectra for the two distinct

sites. D) Low to high magnification SEM images of the same site obtained after rapid cryo-fixation of the sample to preserve structural features of the nano-bio composites on the cell surface with the typical spherical shape and size of up to few microns (bottom image). E) SR μXRF elemental maps together with atomic number (Z) and density-sensitive STXM [59] performed on the same site showing the extensive binding of biomolecules and essential minerals C, N, O, Na and Mg on the Ti-rich local regions. Typical XRF spectra collected from an image pixel on the nano-bio composite and its fits for individual elements (color-coded) is presented in the bottom chart. F) Correlative live cell CLSM and high-vacuum SEM and μXRF reveal a high content of biomolecules inside morphologically distinct TiO_2 composites (white arrows).

To further elucidate the intricate structural and functional properties of the studied biological matter-nanoparticle interface at the nanoscale, we implemented a combined multimodal confocal fluorescence microscopy technique performed on live cells, in conjunction with SR μXRF and ultra-high resolution helium ion microscopy (HIM) with high surface sensitivity performed on fixed cells for the first time (Fig. 4).

By using targeted fluorescence labelling prior to live cell imaging of lung epithelial LA4 cells that had been exposed to TiO_2 NTs for a period of two days, it was possible to image and characterize in detail specific sites where structures had formed on the cell surface (Fig. 4A-B). Large, up to a few microns in size, structures of condensed TiO_2 NTs and biological material, with a roughly spherical shape, were observed in detail in the 3D fluorescence image. Furthermore, additional fHSI and FLIM imaging was performed at the same site (Fig. 4B), allowing for the investigation of heterogeneity and the differentiation of the distinct molecular environments around the reporting fluorophores attached to the observed structure [3]. While fHSI showed no significant spectral changes across the composite, indicating the absence of specific local molecular variations and physical properties in the immediate nm neighbourhood, FLIM, revealed significant fluctuations in the fluorescence decay between different local sites. The orange and blue rectangles indicate sites with fluorescence lifetimes (τ_m) that differ by more than a factor of two. This may indicate on different degrees of dye aggregation/self-quenching [60], but more detailed study is required.

To gain a deeper insight into the underlying cause of the observations, the sample was cryo-fixed immediately after fHSI/FLIM imaging and subsequently transferred to high vacuum SR μXRF and ultra-high resolution HIM for the purpose of conducting chemical and morphological analysis, respectively, on the same structure. The use of a Si_3N_4 substrate as an optimal fiducial marker enabled the rapid registration of the same site. Chemical speciation and detailed surface

examination provided new insights that now better explain the differences in the molecular environment observed in living cells (Fig. 4C-E). Highly sensitive, sub-micron resolution SR µXRF revealed the presence of localized, highly concentrated iron (Fe) (indicated by the dashed rectangle), in addition to widely distributed titanium (Ti), oxygen (O) and carbon (C), the latter from hydrocarbons in the biological material. Overlaying the data from the three techniques used, namely FLIM, SR µXRF and HIM (Fig. 4E, bottom right), it is evident that there is a remarkable co-localization of the shortened fluorescence lifetime (in red) with the increased Fe content (in purple). Only by applying a correlative microscopy approach it was possible to confirm that the local changes in the molecular environment, as measured by FLIM, were most likely due to the presence of highly concentrated Fe particles. In addition to TiO_2 and laser illumination, these could potentially induce a higher localized surface plasmon resonance (LSPR) [61,62] than at the remaining sites, resulting in a shorter fluorescence lifetime [63]. Conversely, Fe can interact with nearby lipids and proteins, catalyzing lipid peroxidation [64], inducing bilayer disruption, an increase in water permeability and thus an increase in membrane polarity [65], resulting in a shortening of the dye lifetime. Further studies are required to gain a more detailed understanding of the Fe-induced changes in the molecular environment.

The implementation of correlative HIM allowed further identification of the distinctive shape and topographic features in the region of localized high Fe content (Fig. 4C, inset). The surface shows a more compact and flat topography with nm-scale roughness. In addition, ultra-high resolution HIM imaging revealed another distinct feature in the center of the object, resembling a 'wormhole' or tunnel (inset on the right). This void space was formed during the assembly of a nano-bio composite and could potentially be used for the diffusion and exchange of organic matter between the inside and outside of the cell. This type of nano-bio interface assembly with the revealed nm features has never been demonstrated before and could be an interesting subject of further investigation.

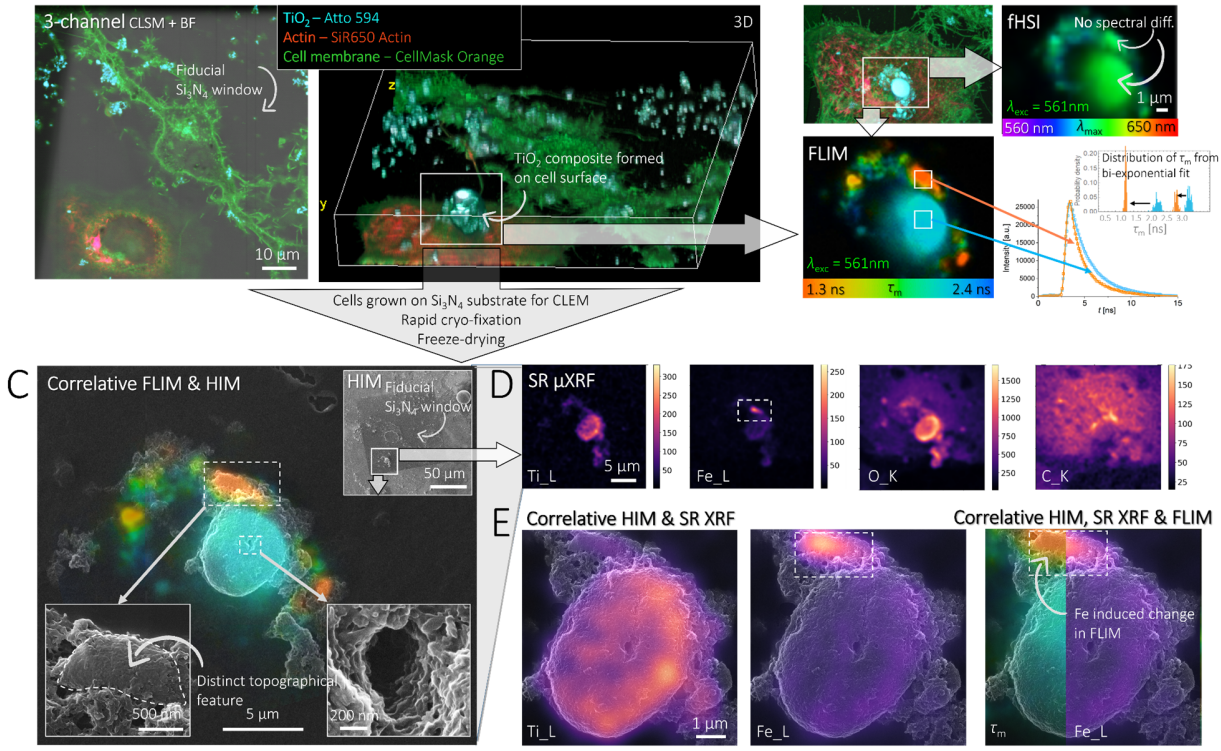

Fig. 4. Novel high-resolution CLEM-µXRF reveling heterogeneity and linked structural and functional properties of TiO_2 NPs-rich cell-compacted and/or cell-excreted composites on the plasma membrane of lung epithelial LA-4 cells. A) Cell growth on thin Si_3N_4 window (in gray, bright field microscopy BF) and labeled cell membranes (in green), actin network (in red) and nanoparticles (in blue) acquired with 3-channel CLSM using 60X water immersion objective. 3D CLSM reveals size, shape and topography of a large, few micron-sized nano-bio composite formed on the surface (marked with an arrow). B) fHSI and FLIM imaging and analysis of the investigated composite reveal no particular spectral contrast, but significant contrast in fluorescence lifetime, respectively (see the charts on the right). C) Correlative FLIM and HIM exhibit co-localization of distinct fluorescence lifetime of investigated dyes with distinct nanoscale topographical features (left inset) where HIM provides more than two-orders of magnitude higher imaging resolution. Another distinct feature in shape of void space or tunnel in the center of the nano-bio composite object is shown on the right inset. D) SR µXRF elemental maps of metals and biomolecules distributed throughout the investigated cellular region. E) Changes in the molecular environment on the nano-bio interface are plausibly caused by high Fe content measured by correlative HIM, SR µXRF and FLIM, the CM approach applied for the first time.

As a final example of our study using novel correlative microscopy techniques on a nano-bio interface, we present another intriguing feature that has developed locally over a large aggregated nano-bio composite: a thin fibrous network of biological matter (Fig. 5D). The organization and

thickness of the fibers, which are on the order of a few tens of nanometers, are consistent with a fibrin origin [66,67]. Given that fibrin fibers have been found to accumulate excessively in the early stages of acute lung injury [68,69], the potential presence of fibrin in our studied system could have significant implications for the local initiation of acute epithelial injury induced by TiO_2 NTs. Nevertheless, further investigation is required to confirm the injury and potential long-term inflammation, particularly with regard to the development of such structures over time.

In addition to the structures observed by high magnification SEM, the nano-bio composite was characterized on live cells using 3-channel CLSM in both 2D and 3D (Fig. 5A). Furthermore, FLIM was performed to investigate changes in the surrounding microenvironment of the excited Atto594 and Draq5 dyes, attached to TiO_2 NTs and DNA, respectively (Fig. 5B). FLIM revealed a high degree of heterogeneity in the fluorescence decay times of Atto594. The average decay time τ_m, calculated from a bi-exponential fit, was approximately half shorter in localized regions (in yellow) than in the rest of the sample (in blue). Correlative SR µXRF was performed on the same site, which showed a co-localization between the short fluorescence decay site and the high Fe site (Fig. 5E-F). This finding is analogous to that shown in Fig. 4. This lends considerable weight to the hypothesis that a locally higher surface plasmon resonance is a very likely explanation [61]. However, due to slight displacement or shrinkage of the system during rapid cryo-fixation, the colocalization is not perfect in this case (Fig. 5F).

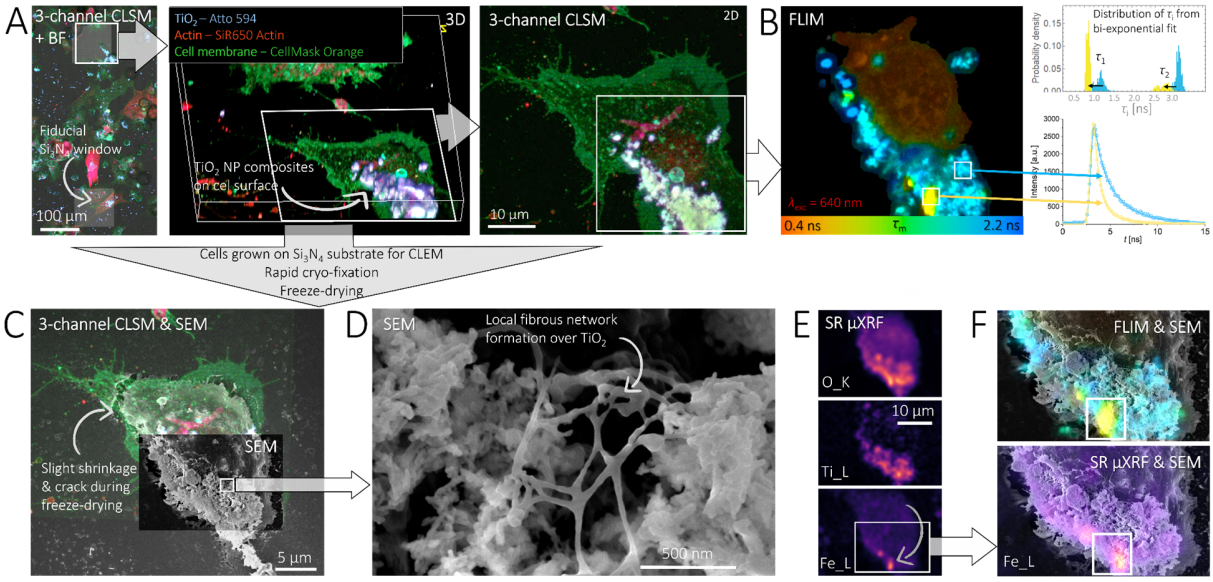

Fig. 5. Novel high-resolution CLEM-µXRF confirming Fe-induced changes in the molecular environment and reveling fibrous network resembling fibrin matrix locally formed over TiO_2 NPs-rich nano-bio composites

anchored on the plasma membrane of lung epithelial LA-4 cells. A) Cell growth on thin Si_3N_4 windows (in gray) and labeled cell membranes (in green), actin network (in red) and nanoparticles (in blue) acquired with 3-channel CLSM using 10X and 60X water immersion objective. High-magnification 2D and 3D CLSM reveal size, shape and topography of a large, few micron-sized nano-bio composite formed on the surface (marked with an arrow). B) FLIM imaging and analysis of the investigated composite reveal significant contrast in fluorescence lifetime between local regions (from yellow to blue) and presented in the charts on the right. C) Correlative CLSM and SEM shows slight shrinkage and local cracks in the periphery of cells after rapid freeze-drying but, most importantly, preserve the investigated structures on cellular surface. D) Local formation and the morphology of fibrous network formed over the nano-bio composites aggregated on the cellular surface. E) SR µXRF elemental maps of metals and oxygen distributed throughout the investigated cell. F) Confirmation of very likely Fe-induced local changes on the nano-bio interface (inset regions) measured by correlative FLIM, SR µXRF and SEM.

3. Conclusion

In this study, we highlight the importance of implementing novel multimodal and multiscale CLEM approaches that elucidate the intricate interactions between biological matter of a model lung epithelium and nanoparticles at a nanoscale resolution. The study provides comprehensive insights into the structural and functional dynamics of the nanoparticle-cell interface, as well as insight into the UFP-induced lung epithelial nanotoxicity, by integrating multimodal live cell imaging with high-resolution high-vacuum light, electron and ion imaging performed on the same cellular site. By combining fluorescence lifetime imaging microscopy (FLIM), hyperspectral fluorescence imaging (fHSI) and high-vacuum scanning electron microscopy (SEM), as well as novel ultra-high resolution helium ion microscopy (HIM) and synchrotron micro X-ray fluorescence (SR µXRF), which were applied for the first time, we were able to observe and characterize the morpho-functional changes in nano-bio composites upon exposure to TiO_2 nanotubes (TiO_2 NTs). The main results are as follows:

- Nanoparticle localization and aggregation on lung epithelial surface: TiO_2 NTs anchor on the cell membrane surface which validates the results of our previous study [35]. The aggregates are characterized with distinct morphology and size heterogeneity (nm – few µm).
- Implications for apoptosis and inflammation: the results suggest that the high DNA content in large extracellular vesicles containing TiO_2 NTs may resemble immobile apoptotic bodies and potentially trigger inflammation.

- Implication for acute injury: the local formation of a fibrous network over anchored nano-bio composites resembles fibrin fibers that may initiate acute epithelial injury.
- Physico-chemical properties of the nano-bio interface and its molecular interactions: extensive binding of biomolecules and essential minerals such as C, N, Na and Mg to TiO_2 NTs, and Fe-induced changes in the local molecular environment measured by FLIM, which is sensitive to the observed FRET and LSPR processes.

The correlative microscopy approach presented is therefore important for studying the initial cellular responses to nanoparticles at such a small scale. These responses play a critical role in the body's initial immune response and the development of inflammation. The methodology provides a robust framework for future research into nanoparticle toxicity and its implications for human health. By addressing key mechanisms at the molecular level and providing high-resolution visualization of nano-bio interactions, this research paves the way for more accurate and reliable interpretations of how nanoparticles affect biological systems, potentially leading to improved safety standards.

4. Material and methods

4.1. Material

The LA-4 murine epithelial lung tissue cell line (ATCC CCL-196), F-12K medium (Gibco), Fetal bovine serum (ATCC), 1% Penicillin-Streptomycin (Sigma), 1% non-essential amino acids (Gibco), Phosphate buffer saline (PBS), Live Cell Imaging Solution (LCIS, Invitrogen); Titanium dioxide nanotubes (TiO_2 NTs) in anatase form synthesized in-house [70]; µ-Slide 8-well (Ibidi), Silicon Nitride Si_3N_4 Support Film (PELCO, 21509CL, Ted Pella), TEM formvar/carbon film on Au Gilder 200 F1 finder grids (FCF200F1-AU-50, EMS), Ammonium acetate (Sigma-Aldrich), PTFE coated high precision and ultrafine tweezers (72919-3SATe, EMS), propane transfer system for plunge freezer (37015, Electron Microscopy Sciences); AlexaFluor 647 (Thermo Fischer Scientific), Atto 594 (ATTO-TEC), CellMask Orange (Invitrogen), SiR-actin (Spirochrome), Draq5 (Invitrogen), MitoTracker™ Orange CMTMRos (Invitrogen), PSM-39 (in-house).

4.2. Cell culture

The LA-4 murine epithelial lung tissue cells were cultured in 75 cm² TPP cell culture flasks. They were maintained in a controlled environment at 37°C with 5% CO_2 and humidity using F-12K

medium supplemented with 15% fetal bovine serum, 1% penicillin-streptomycin and 1% non-essential amino acids. Upon reaching 70-90% confluency at the appropriate passage, the cells were seeded onto specially designed imaging holders customized for correlative microscopy. To enable both, reflection and transmission imaging modes, thin Silicon Nitride (Si_3N_4) and formvar/carbon on Au Gilder 200 F1 finder grid support films were used.

4.3. Nanoparticles

TiO_2 nanoparticles have been selected for investigation in this study due to the potential risks to human health associated with inhalation or oral exposure [71,72]. In case of their high specific surface area, recent studies have demonstrated the potential for these nanoparticles to elicit an inflammatory response [35,73] and to possess carcinogenic properties [36,74]. TiO_2 nanotubes (TiO_2 NTs) in anatase form synthesized in-house with the protocol described in [70] exhibited a diameter range of 6 to 11 nm, a mean length of 100-500 nm, and a BET surface area of 150 m^2 g^{-1} [73]. In order to facilitate enhanced visualization and monitoring of nanomaterial interactions and their impact on model lung epithelium at the sub-micron scale, the TiO_2 NTs were functionalized with super-resolution compatible fluorescent probes, AlexaFluor 647 and Atto 594, according to the protocol described in [43]. Functionalized and filtered nanoparticles suspension was stored in a 100-fold diluted bicarbonate buffer (5 mOsm L^{-1}) prior administration to cells.

4.4. Sample preparation for live-cell confocal fluorescence microscopy

After reaching 70-90% confluency in culture flasks, LA-4 cells were reseeded directly onto UV-sterilized Si_3N_4 or formvar/carbon Au finder grid substrates/holders placed within the chamber of a μ-Slide 8-well. The volume of the added cell suspension prepared at a concentration of a few 10^5 cells/ml was 20 μl and resulted in approximately 5,000 cells per holder with a diameter of 3 mm. Following a four-hour period during which sufficient cell attachment to the substrate had occurred, cell growth media was added to each chamber in order to cover the surface and wet the entire holder, thus preventing any evaporation during the course of the measurements. Once the desired confluency of approximately 50% had been reached (typically within two days), gently sonicated (Bransonic ultrasonic cleaner, Branson 2510 EMT) nanoparticle suspension and carefully rinsed onto the cell monolayer at an average calculated surface dose of 5:1 ($S_{nanomaterial}$:S_{cells}) and total 3 μg/cm². This was achieved by pouring V = 5 μl of a suspension of nanoparticles (c = 0.5 mg/ml) into the chambers of 1 cm² size filled with the cell growth media (V = 300 μl). To put into perspective, the surface dose, which is the most important determinant in the nanomaterial toxicity in lungs [75], was used to be equivalent to exposure over a period of 45

working days, based on the 8-hour time-weighted average occupational exposure limit for TiO_2 (6.0 mg/m^3 TiO_2) established by Danish Regulations [76]. The cells were exposed to nanoparticles for the desired period of time, which was one to three days, prior to live-cell imaging and following cryopreservation for high-vacuum imaging.

Before live-cell imaging, cells were stained with different highly-specific fluorescent dyes to visualize different cell compartments potentially interacting or responding to exposed nanoparticles. Staining was performed according to the manufacturer's recommendations to achieve sufficient fluorescent signal while preserving cellular functions. SiR Actin dye in concentration c = 400 nM was used for 4 h to stain F-actin. Draq 5 dye in concentration c = 5 μM was used for 15 min to stain double-stranded DNA. CellMask Orange in 1000X diluted stock concentration was used for 10 min to stain cell plasma membrane. Mitotracker Orange in concentration 500 nM was used for 15 min to stain mitochondria. All staining solutions were removed and sample was rinsed a few times with LCIS prior measurements performed on the microscope inside the stage top incubator with a temperature, gas and humidity control (H301-MINI, Okolab). Before measurements, the implemented holders with the adhered cells were flipped to enable imaging with small working distance (high numerical aperture) objective. Sterilized polystyrene microspheres of 20 μm in size were employed as volume spacers in order to prevent any compression of the sample.

4.5. Sample preparation for high-vacuum electron and ion microscopy

Immediately after live-cell imaging, sample was carefully transferred from the measuring μ-Slide 8-well into the 150 mM ammonium acetate washing solution to eliminate buffer salt crystals, which otherwise interfere with both structural and chemical analysis performed with high-vacuum techniques [55]. After few seconds of immersion in the washing solution for three times, an excess of water was removed by careful blotting the sides of the sample holder with a lint-free paper. Immediately after blotting, samples were rapidly cryofixated without chemical fixation, to preserve the integrity and morphology of cellular structures and interacting nano-bio interface on the nanoscale, using plunge freezing in a liquid propane to prevent the formation of crystalline ice [77] and stored in a cryo bank until the final drying procedure in a freeze dryer (Coolsafe 100-9 Pro). Propane was prepared in a liquid nitrogen-cooled chamber with the plunge freezer transfer system. To carefully handle with the fragile specimens, high precision cryogenic and non-sticking PTFE tweezers were used. In case of chemical fixation, ammonium acetate washing solution was changed with 4% paraformaldehyde (PFA) and 2% glutaraldehyde (GA) solution. Samples were fixated for 15 minutes at room temperature before blotting and rapid cryofixation.

4.6. Confocal laser scanning microscopy (CLSM)

The experiments were conducted on a custom-built inverted microscope (Olympus IX83) with super-resolution stimulated emission depletion (STED) unit (Abberior Instruments). Imaging was conducted with Olympus 10x (*NA* = 0.3) and 60x (*NA* = 1.2) water immersion objectives, utilizing two pulsed ps lasers in conjunction with a fast-gating system, which was controlled by an FPGA unit. In order to facilitate the simultaneous detection of the fluorescence emitted by different fluorophores, two pulsed diode lasers were employed, with wavelengths of 561 nm and 640 nm, respectively, and a pulse length of 120 ps and repetition rate of 80 MHz. Fluorescence was detected in a descanned mode using an additional pinhole to reduce out-of-focus light and avalanche photodiodes (APD, SPCM-AQRH, Excelitas) with a photon detection efficiency (PDE) exceeding 50% across the entire visible spectrum. Fluorescence was collected from each scanning voxel using a dwell time of 10 µs and detected within the spectral windows λ = 580 - 625 nm and λ = 650 - 720 nm, utilizing dichroics and band-pass filters (both Semrock). For more comprehensive illustration of the optical setup, please refer to the schematics in Fig. S1 of the Supporting Information.

4.7. Fluorescence lifetime imaging microscopy (FLIM) and fluorescence hyperspectral imaging (fHSI)

The microscope system was upgraded with the 16-channel Multi-Wavelength Photo-Multiplier Detectors (PML-16 GaAsP, Hamamatsu), a multi-dimensional Time Correlated Single Photon Counting (TCSPC) detection system and a DCC-100 detector controller card (all manufactured by Becker&Hickl), all communicated through fast ps FPGA electronics, enabling the simultaneous detection of signals across up to 16 spectral channels and detection of their corresponding fluorescence lifetime decays [78]. For fluorescence lifetime imaging, the signals collected on the 16 GaAsP detectors that arrived in the same time interval were summed and the FLIM decay curves obtained in each pixel of the image analyzed using the SPCImage5.0 software (Becker&Hickl) as done before [79,80]. The analysis of FLIM decay curves was conducted using a two-component, double exponential fitting method convoluted with the instrument response function (IRF), which constrains the achievable resolution to its 200 ps FWHM. The pixel exposure time (100 µs) and image binning (3x3) were set to obtain a sufficient peak value of the decay curves of at least 1000 to eligibly resolve fitting with a double-exponential model:

$$I(t) = a_1 e^{-t/\tau_1} + a_2 e^{-t/\tau_2} \quad (1)$$

with the lifetime values of the fast and slow decay components, τ_1 and τ_2, and the corresponding intensity coefficients, a_1 and a_2. The fitted FLIM decay curves from each pixel were color-coded according to the average fluorescence lifetime $\tau_m = a_1\tau_1 + a_2\tau_2$, with the fastest decays shown in red and longer decays in blue. Furthermore, fHSI was conducted utilizing 16 spectral channels within the wide spectral window spanning from 560 nm to 760 nm, as determined by the diffraction grating positioning within the spectrograph (PML-Spec, Becker&Hickl). The high quantum efficiency of approximately 50% across the whole visual spectrum was achieved by GaAsP PMT detectors. The total number of photon counts collected on TCSPC for each pixel was calculated for each spectral channel and represented in the spectral curve. To avoid partial blocking of photons on the notch filters in our de-scanned detection setup which distorts the acquired fluorescence spectra, an optical bypass for collected photons was developed using a combination of acousto-optic tunable filters (AOTF, Opto-electronic) (Fig. S1). The hyperspectral data were fitted by a suitable spectral model, namely the most convenient empirical log-normal function due to its numerical stability during optimization [54]:

$$I_{\mathrm{LN}}(\lambda) = \begin{cases} \exp\left(-\frac{\log 2}{4a^2}\left[log\left(\frac{4a}{w}(\lambda - \lambda_{\max})\right) + 1\right]^2\right), & \lambda > \lambda_{\max} - \frac{w}{4a} \\ 0, & \lambda \leq \lambda_{\max} - \frac{w}{4a} \end{cases} \quad (2)$$

with peak position (λ_{max}), approximate full width at half-maximum (FWHM, w) and asymmetry (a). The developed model was demonstrated to be capable of resolving changes in the spectra as small as 1 nm [54]. Pixel binning of 3x3 was employed prior to spectral fitting, increasing sensitivity at the cost of image resolution.

4.8. Scanning electron microscopy with energy-dispersive X-ray spectroscopy (SEM-EDS)

High-resolution imaging and chemical analysis were conducted in the FEI Helios Nanolab 650 scanning electron microscope (SEM) utilizing energy-dispersive X-ray spectroscopy (EDS). To prevent the charging effects of a highly insulating biological specimen during electron irradiation, all samples were coated with an approximately 10 nm carbon layer. The EDS spectra were collected with the following experimental parameters: electron acceleration voltage (15 kV), electron current (200 pA), and chamber vacuum (10^{-6} hPa). Under these conditions, an energy resolution of 145 eV at the Mn Kα line and an elemental sensitivity of approximately 0.01 wt% (X-Max SDD, Oxford Instruments) were achieved. The weight percentage (wt%) of each individual element was calculated and subsequently employed for further analysis, which entailed the

measurement of the differences in the wt% ratios of the studied elements between individual regions.

4.9. Helium Ion Microsopy (HIM)

High-resolution images at the nanoscale were obtained using a helium ion microscope (Orion NanoFab, Zeiss) [81]. For imaging purposes, He atoms are ionized in the GFIS source. The source is characterized by a small virtual source size (0.25mm), a high reduced brightness (1-4 10^9 $Am^{-2}sr^{-1}V^{-1}$) and a very small energy spread of less than 1 eV. Subsequently the beam is focused, shaped and scanned over the sample surface using electrostatic lenses, quadrupoles, and octapoles. The resulting focused ion beam [82] has a diameter of 0.5 nm and enables the recording of images with a large depth of focus [83]. Prior to imaging, the freeze-dried samples grown on Si_3N_4 substrate were affixed with carbon tape to the standard pins compatible with a multi-pin specimen mount. Insulating samples were spared of conventional thin layer conductive coating due to efficient charge compensation within HIM instrument using the flood gun [84], thus preventing any surface modification at the nanoscale studied. Imaging was conducted through the detection of secondary electrons (SE1) emitted from the few nm surface layer of the sample. The following experimental parameters were employed: helium ion energy (30 keV), ion current (0.5 pA) and chamber vacuum ($2x10^{-7}$ hPa). The field of view (FoV) of the acquired images ranged from less-magnified, 175 µm by 175 µm required for registration, to highly-magnified, 0.7 µm by 0.7 µm, with a minimal pixel step size of 0.7 nm and typical dwell time 20 µs at each pixel.

4.10. Synchrotron Micro-X-ray Fluorescence (SR µ-XRF)

The X-ray fluorescence (XRF) data were collected at the TwinMic beamline of Elettra Sincrotrone Trieste, located in Trieste, Italy [85]. The TwinMic microscope was operated in scanning transmission mode, whereby the sample was raster scanned across an incoming perpendicular X-ray beam, delivered by a zone plate diffractive optics. During the scanning process, a rapid readout charge-coupled device (CCD) camera (DV 860, Andor Technology) collected the transmitted X-ray photons, resulting in the generation of absorption and differential phase contrast images [59]. Simultaneously, the emitted X-ray fluorescence (XRF) photons were collected by eight silicon drift detectors (SDD) situated in front of the sample at an angle of 20 degrees with respect to the sample plane [86]. This results in the simultaneous acquisition of both, the morphology of the sample and the distribution of the elements.

In order to achieve optimal excitation of Mg, Na, O, Ti and C, while also obtaining sub-micron spatial resolution, a monochromatic energy of 1.5 keV was selected for the experiment. The

specimens were scanned at a step size of 500 nm with a probe size of 600 nm in diameter, delivered by an Au zone plate of 600 µm diameter and 50 nm outermost zone width. An acquisition time of 50 ms pixel^{-1} and 4 s pixel^{-1} were employed for the CCD and SDD detector systems, respectively. The acquired XRF spectra were processed using the PyMCA software [87].

Acknowledgements

This work was supported by Helmholtz European Partnering project CROSSING (Grant No: PIE-0007), EU H2020 project no. 824096 “RADIATE”, the Slovenian research and innovation agency (ARIS) programs P1-0060 (Experimental biophysics of complex systems), P1-0112, I0-0005 and projects N1-0090, L7-4535 and N1-0240. The authors thank Prof. Dr. Katarina Vogel Mikuš of the Biotechnical Faculty (University of Ljubljana) for her invaluable assistance with the freeze-drying of samples, Dr. Valentina Bonanni of the Elettra Sincrotrone (Trieste, Italy) for help with the SR µXRF measurements, Prof. Dr. Janez Štrancar of the Jožef Stefan Institute (Ljubljana, Slovenia) for initiating the scientific field in the Laboratory of Biophysics, Dr. Tilen Koklič for fruitful discussions, Dr. Iztok Urbančič for the hyperspectral analysis software support, DR. Stane Pajk for the synthesis of lipid droplet dye, Dr. Polona Umek for synthesis of TiO_2 nanoparticles and Dr. Hana Kokot for fluorescence labeling of TiO_2 nanoparticles (all of the Jožef Stefan Institute).

Author contributions

R.P. conceptualized and designed the analysis; R.P., A.K., L.P. and A.G. performed the experiments; R.P., L.H. and A.G. collected the data; R.P. performed the analysis and data visualization; R.P., G.H. and A.G. contributed analysis tools; R.P. wrote the paper; R.P., L.P., G.H., A.G. and P.P. reviewed and edited the paper; P.P. acquired funding.

References

1. Correlative Light and Electron Microscopy IV, Volume 162 - 1st Edition.
2. Ando, T. *et al.* The 2018 correlative microscopy techniques roadmap. *J. Phys. D: Appl. Phys.* 51, 443001 (2018).
3. Datta, R., Heaster, T. M., Sharick, J. T., Gillette, A. A. & Skala, M. C. Fluorescence lifetime imaging microscopy: fundamentals and advances in instrumentation, analysis, and applications. *J Biomed Opt* 25, 1–43 (2020).
4. Sekar, R. B. & Periasamy, A. Fluorescence resonance energy transfer (FRET) microscopy imaging of live cell protein localizations. *J Cell Biol* 160, 629–633 (2003).
5. Varsano, N. & Wolf, S. G. Electron microscopy of cellular ultrastructure in three dimensions. *Current Opinion in Structural Biology* 76, 102444 (2022).
6. Nuñez, J., Renslow, R., Cliff, J. B. & Anderton, C. R. NanoSIMS for biological applications: Current practices and analyses. *Biointerphases* 13, 03B301 (2017).
7. De Samber, B. *et al.* Effect of sample preparation techniques upon single cell chemical imaging: A practical comparison between synchrotron radiation based X-ray fluorescence (SR-XRF) and Nanoscopic Secondary Ion Mass Spectrometry (nano-SIMS). *Anal Chim Acta* 1106, 22–32 (2020).
8. Manisalidis, I., Stavropoulou, E., Stavropoulos, A. & Bezirtzoglou, E. Environmental and Health Impacts of Air Pollution: A Review. *Front Public Health* 8, 14 (2020).
9. Moreno-Ríos, A. L., Tejeda-Benítez, L. P. & Bustillo-Lecompte, C. F. Sources, characteristics, toxicity, and control of ultrafine particles: An overview. *Geoscience Frontiers* 13, 101147 (2022).
10. Hill, W. *et al.* Lung adenocarcinoma promotion by air pollutants. *Nature* 616, 159–167 (2023).
11. Kempen, P. J. *et al.* A correlative optical microscopy and scanning electron microscopy approach to locating nanoparticles in brain tumors. *Micron* 68, 70–76 (2015).

12. Han, S. *et al.* High-Contrast Imaging of Nanodiamonds in Cells by Energy Filtered and Correlative Light-Electron Microscopy: Toward a Quantitative Nanoparticle-Cell Analysis. *Nano Lett.* 19, 2178–2185 (2019).
13. Hayashi, Y. *et al.* Differential Nanoparticle Sequestration by Macrophages and Scavenger Endothelial Cells Visualized in Vivo in Real-Time and at Ultrastructural Resolution. *ACS Nano* 14, 1665–1681 (2020).
14. García-Serradilla, M. & Risco, C. Light and electron microscopy imaging unveils new aspects of the antiviral capacity of silver nanoparticles in bunyavirus-infected cells. *Virus Research* 302, 198444 (2021).
15. Kopek, B. G. *et al.* Diverse protocols for correlative super-resolution fluorescence imaging and electron microscopy of chemically fixed samples. *Nat Protoc* 12, 916–946 (2017).
16. Gallagher-Jones, M. *et al.* Correlative cellular ptychography with functionalized nanoparticles at the Fe L-edge. *Sci Rep* 7, 4757 (2017).
17. Liu, M. *et al.* Real-time visualization of clustering and intracellular transport of gold nanoparticles by correlative imaging. *Nat Commun* 8, 15646 (2017).
18. Bhat, S. V. *et al.* Correlative atomic force microscopy quantitative imaging-laser scanning confocal microscopy quantifies the impact of stressors on live cells in real-time. *Sci Rep* 8, 8305 (2018).
19. Lo Giudice, C. *et al.* Nanophysical Mapping of Inflammasome Activation by Nanoparticles via Specific Cell Surface Recognition Events. *ACS Nano* 16, 306–316 (2022).
20. Le Trequesser, Q. *et al.* Single Cell In Situ Detection and Quantification of Metal Oxide Nanoparticles Using Multimodal Correlative Microscopy. *Anal. Chem.* 86, 7311–7319 (2014).
21. Podlipec, R. *et al.* Revealing Inflammatory Indications Induced by Titanium Alloy Wear Debris in Periprosthetic Tissue by Label-Free Correlative High-Resolution Ion, Electron and Optical Microspectroscopy. *Materials* 14, 3048 (2021).

22. Quintana, C. *et al.* Morphological and chemical studies of pathological human and mice brain at the subcellular level: Correlation between light, electron, and nanosims microscopies. *Microscopy Research and Technique* 70, 281–295 (2007).
23. Audinot, J.-N. *et al.* Identification and localization of nanoparticles in tissues by mass spectrometry. *Surface and Interface Analysis* 45, 230–233 (2013).
24. Vollnhals, F. *et al.* Correlative Microscopy Combining Secondary Ion Mass Spectrometry and Electron Microscopy: Comparison of Intensity–Hue–Saturation and Laplacian Pyramid Methods for Image Fusion. *Anal. Chem.* 89, 10702–10710 (2017).
25. Lovric, J., Audinot, J.-N. & Wirtz, T. In situ Correlative Helium Ion Microscopy and Secondary Ion Mass Spectrometry for High-Resolution Nano-Analytics in Life Sciences. *Microscopy and Microanalysis* 25, 1026–1027 (2019).
26. Biesemeier, A. *et al.* Correlative Electron Microscopy, High Resolution Ion Imaging and Secondary Ion Mass Spectrometry for High Resolution Nanoanalytics on Biological Tissue. *Microscopy and Microanalysis* 26, 818–820 (2020).
27. De Castro, O. *et al.* npSCOPE: A New Multimodal Instrument for In Situ Correlative Analysis of Nanoparticles. *Anal. Chem.* 93, 14417–14424 (2021).
28. Le Trequesser, Q. *et al.* Multimodal correlative microscopy for in situ detection and quantification of chemical elements in biological specimens. Applications to nanotoxicology. *J Chem Biol* 8, 159–167 (2015).
29. James, S. A. *et al.* Quantification of ZnO Nanoparticle Uptake, Distribution, and Dissolution within Individual Human Macrophages. *ACS Nano* 7, 10621–10635 (2013).
30. Tardillo Suárez, V. *et al.* Correlative transmission electron microscopy and high-resolution hard X-ray fluorescence microscopy of cell sections to measure trace element concentrations at the organelle level. *Journal of Structural Biology* 213, 107766 (2021).
31. Malucelli, E. *et al.* Quantitative chemical imaging of the intracellular spatial distribution of fundamental elements and light metals in single cells. *Anal Chem* 86, 5108–5115 (2014).

32. Perrin, L., Carmona, A., Roudeau, S. & Ortega, R. Evaluation of sample preparation methods for single cell quantitative elemental imaging using proton or synchrotron radiation focused beams. *J. Anal. At. Spectrom.* 30, 2525–2532 (2015).
33. Jobim, P. F. C. *et al.* Human Neocortex Layer Features Evaluated by PIXE, STIM, and STXM Techniques. *Biol Trace Elem Res* 201, 592–602 (2023).
34. Pongrac, P. *et al.* Spatially resolved distributions of the mineral elements in the grain of tartary buckwheat (*Fagopyrum tataricum*). *Food Research International* 54, 125–131 (2013).
35. Kokot, H. *et al.* Prediction of Chronic Inflammation for Inhaled Particles: the Impact of Material Cycling and Quarantining in the Lung Epithelium. *Advanced Materials* 32, 2003913 (2020).
36. Podlipec, R. *et al.* Binucleated cell formation and oncogene expression after particulate matter exposure is preceded by microtubule disruption, dysregulated cell cycle, prolonged mitosis, and septin binding. 2024.01.07.574515 Preprint at https://doi.org/10.1101/2024.01.07.574515 (2024).
37. Zhang, Y. *et al.* Quantitating morphological changes in biological samples during scanning electron microscopy sample preparation with correlative super-resolution microscopy. *PLoS One* 12, e0176839 (2017).
38. Li, Y. *et al.* The effects of chemical fixation on the cellular nanostructure. *Exp Cell Res* 358, 253–259 (2017).
39. Murk, J. L. a. N. *et al.* Influence of aldehyde fixation on the morphology of endosomes and lysosomes: quantitative analysis and electron tomography. *Journal of Microscopy* 212, 81–90 (2003).
40. Ebersold, H. R., Cordier, J. L. & Lüthy, P. Bacterial mesosomes: method dependent artifacts. *Arch Microbiol* 130, 19–22 (1981).
41. Idziak, A., Inavalli, V. V. G. K., Bancelin, S., Arizono, M. & Nägerl, U. V. The Impact of Chemical Fixation on the Microanatomy of Mouse Organotypic Hippocampal Slices. *eNeuro* 10, (2023).

42. Parlanti, P. & Cappello, V. Microscopes, tools, probes, and protocols: A guide in the route of correlative microscopy for biomedical investigation. *Micron* 152, 103182 (2022).
43. Kokot, B. *et al.* How to control fluorescent labeling of metal oxide nanoparticles for artefact-free live cell microscopy. *Nanotoxicology* 15, 1102–1123 (2021).
44. Suhling, K. *et al.* Fluorescence Lifetime Imaging. in *Handbook of Photonics for Biomedical Engineering* (eds. Ho, A. H.-P., Kim, D. & Somekh, M. G.) 1–50 (Springer Netherlands, Dordrecht, 2021).
45. Strickfaden, H. Reflections on the organization and the physical state of chromatin in eukaryotic cells. *Genome* 64, 311–325 (2021).
46. Shrestha, D., Jenei, A., Nagy, P., Vereb, G. & Szöllősi, J. Understanding FRET as a Research Tool for Cellular Studies. *Int J Mol Sci* 16, 6718–6756 (2015).
47. Prieto-Vila, M., Yoshioka, Y. & Ochiya, T. Biological Functions Driven by mRNAs Carried by Extracellular Vesicles in Cancer. *Frontiers in Cell and Developmental Biology* 9, (2021).
48. Urbančič, I. *et al.* Nanoparticles Can Wrap Epithelial Cell Membranes and Relocate Them Across the Epithelial Cell Layer. *Nano Lett.* 18, 5294–5305 (2018).
49. Bischoff, M., Biriukov, D., Předota, M., Roke, S. & Marchioro, A. Surface Potential and Interfacial Water Order at the Amorphous TiO2 Nanoparticle/Aqueous Interface. *J. Phys. Chem. C* 124, 10961–10974 (2020).
50. Lenzi, M. *et al.* 6-(Methylsulfonyl) hexyl isothiocyanate as potential chemopreventive agent: molecular and cellular profile in leukaemia cell lines. *Oncotarget* 8, 111697–111714 (2017).
51. Poon, I. K. H., Lucas, C. D., Rossi, A. G. & Ravichandran, K. S. Apoptotic cell clearance: basic biology and therapeutic potential. *Nat Rev Immunol* 14, 166–180 (2014).
52. Gianoncelli, A. *et al.* Soft X-ray Microscopy Techniques for Medical and Biological Imaging at TwinMic—Elettra. *Applied Sciences* 11, 7216 (2021).
53. Solvent and Environmental Effects. in *Principles of Fluorescence Spectroscopy* (ed. Lakowicz, J. R.) 205–235 (Springer US, Boston, MA, 2006).

54. Urbančič, I., Arsov, Z., Ljubetič, A., Biglino, D. & Strancar, J. Bleaching-corrected fluorescence microspectroscopy with nanometer peak position resolution. *Opt Express* 21, 25291–25306 (2013).

55. Berman, E. S. F. *et al.* Preparation of Single Cells for Imaging/Profiling Mass Spectrometry. *Journal of the American Society for Mass Spectrometry* 19, 1230–1236 (2008).

56. Liu, Y., Tan, J., Thomas, A., Ou-Yang, D. & Muzykantov, V. R. The shape of things to come: importance of design in nanotechnology for drug delivery. *Ther Deliv* 3, 181–194 (2012).

57. First-principles study of Na insertion at TiO2 anatase surfaces: new hints for Na-ion battery design. *Nanoscale Advances* 2, 2745–2751 (2020).

58. Farrugia, B. L., Lord, M. S., Melrose, J. & Whitelock, J. M. The Role of Heparan Sulfate in Inflammation, and the Development of Biomimetics as Anti-Inflammatory Strategies. *J Histochem Cytochem* 66, 321–336 (2018).

59. Gianoncelli, A., Morrison, G. R., Kaulich, B., Bacescu, D. & Kovac, J. Scanning transmission x-ray microscopy with a configurable detector. *Applied Physics Letters* 89, 251117 (2006).

60. Lu, M., Kaminski, C. F. & Schierle, G. S. K. Advanced fluorescence imaging of in situ protein aggregation. *Phys Biol* 17, 021001 (2020).

61. Mayer, K. M. & Hafner, J. H. Localized Surface Plasmon Resonance Sensors. *Chem. Rev.* 111, 3828–3857 (2011).

62. Tang, L., Casas, J. & Venkataramasubramani, M. Magnetic nanoparticle mediated enhancement of localized surface plasmon resonance for ultrasensitive bioanalytical assay in human blood plasma. *Anal Chem* 85, 1431–1439 (2013).

63. Li, J. *et al.* Spectral variation of fluorescence lifetime near single metal nanoparticles. *Sci Rep* 6, 21349 (2016).

64. Li, J. *et al.* Ferroptosis: past, present and future. *Cell Death Dis* 11, 1–13 (2020).

65. Danylchuk, D. I., Jouard, P.-H. & Klymchenko, A. S. Targeted Solvatochromic Fluorescent Probes for Imaging Lipid Order in Organelles under Oxidative and Mechanical Stress. *J Am Chem Soc* 143, 912–924 (2021).
66. Ryan, E., Mockros, L., Weisel, J. & Lorand, L. Structural origins of fibrin clot rheology. *Biophys J* 77, 2813–2826 (1999).
67. Li, W. *et al.* Fibrin Fiber Stiffness Is Strongly Affected by Fiber Diameter, but Not by Fibrinogen Glycation. *Biophys J* 110, 1400–1410 (2016).
68. Idell, S. *et al.* Local abnormalities in coagulation and fibrinolytic pathways predispose to alveolar fibrin deposition in the adult respiratory distress syndrome. *J Clin Invest* 84, 695–705 (1989).
69. Idell, S. Coagulation, fibrinolysis, and fibrin deposition in acute lung injury. *Crit Care Med* 31, S213-220 (2003).
70. Garvas, M. *et al.* Protein Corona Prevents TiO2 Phototoxicity. *PLoS One* 10, e0129577 (2015).
71. Baranowska-Wójcik, E., Szwajgier, D., Oleszczuk, P. & Winiarska-Mieczan, A. Effects of Titanium Dioxide Nanoparticles Exposure on Human Health—a Review. *Biol Trace Elem Res* 193, 118–129 (2020).
72. Gutierrez, C. T. *et al.* Acute phase response following pulmonary exposure to soluble and insoluble metal oxide nanomaterials in mice. *Particle and Fibre Toxicology* 20, 4 (2023).
73. Danielsen, P. H. *et al.* Effects of physicochemical properties of TiO2 nanomaterials for pulmonary inflammation, acute phase response and alveolar proteinosis in intratracheally exposed mice. *Toxicology and Applied Pharmacology* 386, 114830 (2020).
74. Wang, J. J., Sanderson, B. J. S. & Wang, H. Cyto- and genotoxicity of ultrafine TiO2 particles in cultured human lymphoblastoid cells. *Mutation Research/Genetic Toxicology and Environmental Mutagenesis* 628, 99–106 (2007).

75. Schmid, O. & Stoeger, T. Surface area is the biologically most effective dose metric for acute nanoparticle toxicity in the lung. *Journal of Aerosol Science* 99, 133–143 (2016).
76. Jackson, P. *et al.* Maternal inhalation of surface-coated nanosized titanium dioxide (UV-Titan) in C57BL/6 mice: effects in prenatally exposed offspring on hepatic DNA damage and gene expression. *Nanotoxicology* 7, 85–96 (2013).
77. Tivol, W. F., Briegel, A. & Jensen, G. J. An Improved Cryogen for Plunge Freezing. *Microsc Microanal* 14, 375–379 (2008).
78. Becker, W. *The Bh TCSPC Handbook 10th Edition, 2023*.
79. Podlipec, R., Mur, J., Petelin, J., Štrancar, J. & Petkovšek, R. Two-photon retinal theranostics by adaptive compact laser source. *Appl. Phys. A* 126, 405 (2020).
80. Podlipec, R., Mur, J., Petelin, J., Štrancar, J. & Petkovšek, R. Method for controlled tissue theranostics using a single tunable laser source. *Biomed Opt Express* 12, 5881–5893 (2021).
81. *Helium Ion Microscopy*. (Springer International Publishing, Cham, 2016). doi:10.1007/978-3-319-41990-9.
82. Höflich, K. *et al.* Roadmap for focused ion beam technologies. *Applied Physics Reviews* 10, 041311 (2023).
83. Hlawacek, G., Veligura, V., van Gastel, R. & Poelsema, B. Helium ion microscopy. *Journal of Vacuum Science & Technology B* 32, 020801 (2014).
84. Schmidt, M., Byrne, J. M. & Maasilta, I. J. Bio-imaging with the helium-ion microscope: A review. *Beilstein J. Nanotechnol.* 12, 1–23 (2021).
85. Gianoncelli, A., Kourousias, G., Merolle, L., Altissimo, M. & Bianco, A. Current status of the TwinMic beamline at Elettra: a soft X-ray transmission and emission microscopy station. *J Synchrotron Radiat* 23, 1526–1537 (2016).
86. Gianoncelli, A., Kourousias, G., Stolfa, A. & Kaulich, B. Recent developments at the TwinMic beamline at ELETTRA: an 8 SDD detector setup for low energy X-ray Fluorescence. *J. Phys.: Conf. Ser.* 425, 182001 (2013).

87. Solé, V. A., Papillon, E., Cotte, M., Walter, Ph. & Susini, J. A multiplatform code for the analysis of energy-dispersive X-ray fluorescence spectra. *Spectrochimica Acta Part B: Atomic Spectroscopy* 62, 63–68 (2007).